

Avalanches of rearrangements in quasi-2D emulsion hopper flow

Xia Hong,^a Kenneth W. Desmond,^b Dandan Chen^{c,d} and Eric R. Weeks^{*a}

We experimentally study the flow of a quasi-two-dimensional emulsion through a constricting hopper shape. Our area fractions range from $\phi = 0.83 - 0.99$, such that the droplets are always in contact with one another and are in many cases highly deformed. At the lowest flow rates, the droplets exit the hopper via intermittent avalanches. At the highest flow rates, the droplets exit continuously. The transition between these two types of behaviors is a fairly smooth function of the mean strain rate. The avalanches are characterized by a power law distribution of the time interval between droplets exiting the hopper, with long intervals between the avalanches. There is little or no dependence of the flow behavior on the area fraction of the system.

1 Introduction

Many slowly strained materials exhibit intermittent flow behavior: long still periods punctuated by rapid avalanches where material flows¹⁻⁵. Examples include diverse phenomena such as earthquakes^{6,7}, general deformations of solids⁸, stick-slip friction due to granular layers^{9,10}, Barkhausen noise in magnetic materials¹¹, and sheep herded through constrictions¹². More commonly, avalanches are seen in slow flows of athermal soft materials such as emulsions¹, bubble rafts¹³, foams^{4,14-17}, and granular materials¹⁸⁻²³. These soft materials typically have amorphous structure, necessitating that flow and rearrangements are disordered on a microscopic scale. The slow flow speed is a key feature: for example, a rotating drum experiment with sand inside demonstrated avalanches at low rotation rates and smooth flow at high rotation rates²⁴. For granular materials, static friction can prevent the material from flowing and can lead to avalanches. In systems composed of fluids such as foams and emulsions, stresses are supported not by static friction but rather surface tension, which resists the deformation of the bubbles or droplets.

In this manuscript, we present an experimental study of a flowing emulsion where we see a range of flow behaviors. Our emulsions are oil droplets in water and are compressed between two parallel glass plates so that the droplets are deformed into pancake-like disks. The area fractions are all above jamming¹⁴, such that the droplets touch each other and are in many cases highly deformed by their neighbors. At the slowest flow rates, we see large avalanches of rearrangements. At higher flow rates rearrangement events are always occurring and droplets exit continuously. Intriguingly, the transition between the two flow behaviors occurs fairly smoothly as the flow rate is increased, and at moderate flow rates we see an

intermediate type of flow behavior. Despite the range of area fractions we study ($\phi = 0.83 - 0.99$), the area fraction does not seem to control the flow behavior.

2 Experimental Method

2.1 Design

Our emulsions are mineral oil droplets in water using Fairy detergent (mass fraction 0.025) as a surfactant to prevent coalescence of the droplets^{25,26}. The droplets are produced using a standard co-flow micro-fluidic technique²⁷. The radius polydispersity of our droplets made this way is 1% (standard deviation divided by mean). To prevent droplets from organizing into crystalline arrays, for each experiment we make a bidisperse emulsion by mixing together two separate batches of monodisperse droplets at a volume ratio of about 1:1. While each individual batch of monodisperse droplets has a low polydispersity, there is some variability between batches. The mean diameter of the large droplets is $270 \pm 50 \mu\text{m}$ and of the small droplets is $200 \pm 40 \mu\text{m}$, and the diameter ratios of the bidisperse mixtures we form are in the range $d_L/d_S = 1.5 \pm 0.2$.

In our experiment, we confine droplets between two 25 mm \times 75 mm glass slides. The slides are separated by pieces of 100 μm transparency film sealed with epoxy. These pieces of film act as spacers and thus creating a gap between the slides. This gap ranges from 115 to 140 μm in different experiments. Nonetheless, within a given sample chamber, this gap is constant with uncertainty 1.8% within any given experiment so the slides are parallel (the corresponding maximum angle between two slides is 1°). The diameters of the oil droplets are chosen to be larger than the gap of the sample chamber. Thus, the droplets are squeezed between the two glass slides without overlapping to achieve a quasi-2D system.

The left panel in Fig. 1 shows the schema of the chamber. The pieces of film are cut to form a symmetric hopper channel with angle $\theta = 54 \pm 5^\circ$ (see Fig. 1) and opening width 0.7 - 1

^a Department of Physics, Emory University, Atlanta, GA 30322 USA

^b ExxonMobil, Amundale, NJ 08801, USA

^c School of Radiation Medicine and Protection, Medical College of Soochow University, Suzhou, China

^d Collaborative Innovation Center of Radiation Medicine of Jiangsu Higher Education Institutions, Suzhou, China

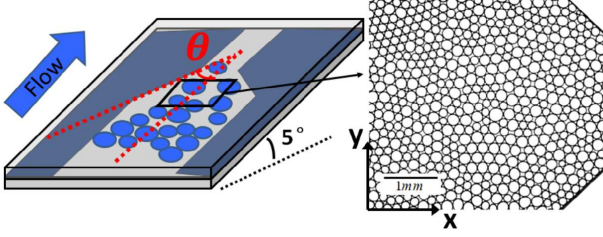


Fig. 1 Schema of the sample chamber (left) and raw image of the emulsion (right).

mm. The sample chamber is tilted at an angle $5 \pm 1^\circ$ relative to the horizontal, to use the buoyant force of the droplets to balance the viscous friction between droplets and glass slides. The buoyant force is due to the density difference between water and mineral oil ($\rho_{\text{water}} = 1.00 \text{ g/cm}^3$, $\rho_{\text{oil}} = 0.83 \text{ g/cm}^3$). First we load the emulsion into the sample chamber, and then behind the emulsion we add pure mineral oil. A syringe pump injects additional mineral oil into the chamber at constant flux rate to push the emulsion through the chamber and thus funnel the droplets through the hopper exit. We use a microscope with a $1.6\times$ objective lens to image the system, focusing on the chamber midplane where the 2D droplet images are clearest. A CCD camera records the images in the region close to (0.5-2 mm away from) the hopper opening. Depending on the mean speed of the flow in a given experiment, the camera frame rate is between 0.2 and 2 images/second. This is sufficient to track the trajectory of each individual droplet using standard software²⁸, even at the maximum velocity $0.06\langle D \rangle/s$, where $\langle D \rangle$ is the mean diameter of the droplets. The right panel in Fig. 1 shows a typical raw image, in which we record hundreds of droplets within the field of view.

2.2 Control Parameters

The two control parameters for our experiments are the area fraction ϕ and the flux rate F . ϕ is the fraction of the area occupied by oil droplets, which is calculated based on the 2D image. We take a total of 45 data sets with $0.83 \leq \phi \leq 0.99$ and $0.0001 \leq F \leq 0.02 \text{ ml/hr}$. From the post-processed images, we observe that ϕ has only minimal fluctuations during an experiment, with a relative standard deviation no more than 0.5%. These fluctuations are primarily due to the finite field of view, with ϕ changing when droplets flow in and out. In flowing suspensions of solid particles there can be a self-filtration effect²⁹, but in our data the mean area fraction as a function of time has no monotonic ascending and thus there is no self-filtration. There is an additional possible systematic uncertainty for ϕ as the apparent size of each droplet depends on the illumination settings of the microscope. We keep these settings constant between each experiment. For each experiment,

F is set by a syringe pump and thus is constant. However, the observed flow velocity fluctuates. This is likely due to some compliance in the sample chamber, allowing sample to flow in slightly without having to flow out, and building up pressure until it is released by droplets flowing out.

To simplify the discussion, rather than focusing on flux, we use the experimentally measured quantity of the mean strain rate $\langle \dot{\gamma} \rangle$. $\langle \dot{\gamma} \rangle$ is defined and calculated as follow. x and y are defined using the coordinate system on the right panel in Fig. 1. For each droplet, we determine the trajectory of its center of mass, $[x(t), y(t)]$. Using a short time interval, we also determine its instantaneous velocity (v_x, v_y) . For a given droplet, we consider the motion of it and its neighbors (defined as those droplets connected by a Delaunay triangulation of all the droplets). Using these data, the instantaneous strain rate of this droplet j is averaged over all neighbors:

$$\dot{\gamma}_j = \left| \left\langle \frac{v_x(j) - v_x(i)}{y_j - y_i} \right\rangle_i \right|, \quad (1)$$

where the subscript i indicates the i th neighbor of the reference droplet j , and the average is taken over all of the neighbors. The strain rate can be interpreted as the spacial gradient in y direction of the velocity in x direction; the gradients of the y velocity are smaller and accordingly we neglect them. The mean strain rate $\langle \dot{\gamma} \rangle$ of each data set is calculated by averaging over all droplets and all time.

3 Results and Discussion

We observe a wide range of flow behaviors as we vary F and ϕ for different experiments. For large F , droplets flow continuously and smoothly (referred as *smooth flow* cases in this article). For small F , we see avalanche-like flow (referred as *avalanche* cases). For intermediate flux rates F , we observe *intermediate cases* between these two flow patterns. As will be discussed below, we do not see any clear dependence of these flow patterns on the area fraction ϕ .

We summarize these three flow behaviors in Fig. 2. The three pictures in Fig. 2(a)-(c) use color to show the time each droplet exits the hopper opening to the right. Red droplets exit the earliest, and blue the latest. The left picture is a smooth flow case, which shows a smooth gradient in color. The right one shows an avalanche case, where droplets have distinct groups of colors indicating that droplets exit the hopper in bursts. Note that the color scale of each plot corresponds to a different amount of time, as specified in the caption.

Figs. 2(d)-(f) quantify these pictures by showing the cumulative number of droplets that have exited the hopper as a function of time for our three flow cases. In the smooth flow case (d), the data form a smooth curve with a well-defined slope, showing that droplets exit the hopper continuously at a fairly

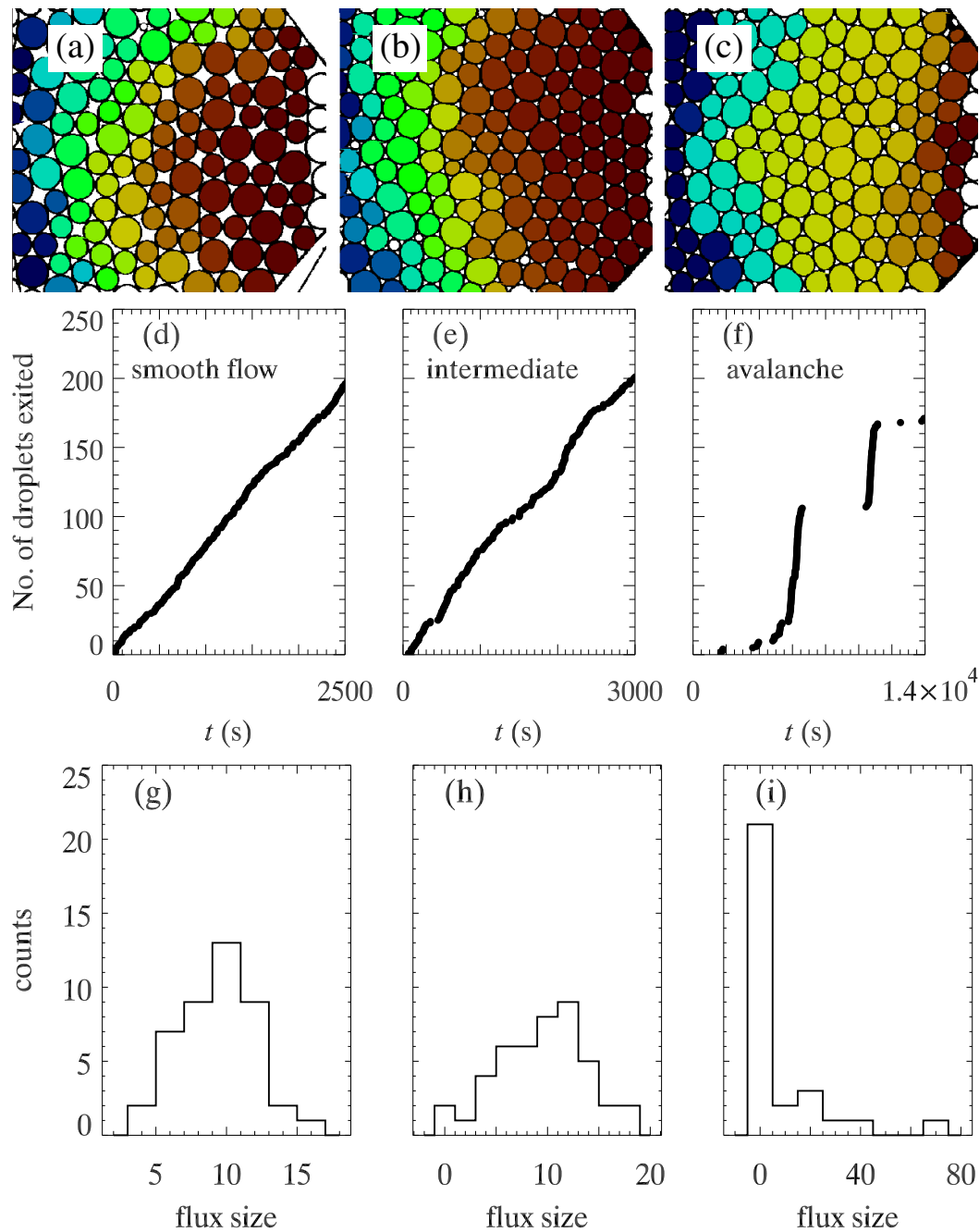


Fig. 2 Description of the three flow behaviors. (a-c) Images of the samples at a particular time, with the color indicating the time when the droplet exits. The red droplets exit earlier and blue droplets exit later. The time ranges for the colors are (a) 1250 s, (b) 3000 s, and (c) 14000 s. (d-f) The number of droplets that have exited the hopper as a function of time. (g-i) Histograms of the number of droplets exiting the hopper within a short time window, chosen such that the mean of the histogram is 10 droplets. The flow conditions are: (a,d,g) smooth flow, $\phi = 0.87$, $\langle \dot{\gamma} \rangle = 0.065 \text{ s}^{-1}$. (b,e,h) Intermediate, $\phi = 0.96$, $\langle \dot{\gamma} \rangle = 0.02 \text{ s}^{-1}$. (c,f,i) Avalanche, $\phi = 0.96$, $\langle \dot{\gamma} \rangle = 0.01 \text{ s}^{-1}$.

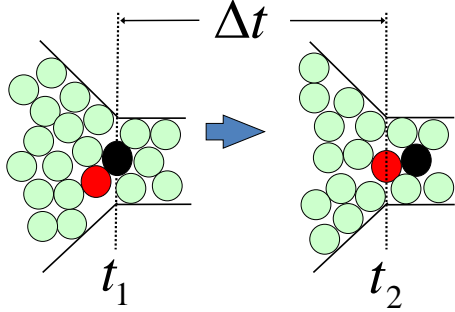


Fig. 3 Schema of the definition of interval Δt . The left figure is at time t_1 when the black droplet exits the hopper. The right figure is at time t_2 when the red droplet exits the hopper.

constant rate. The intermediate case (e) shows fluctuations in the rate, although it is still fairly continuous. In avalanche case (f), there are stretches of time where no droplets exit, followed by discrete sudden flow events where many droplets exit within a short period of time, indicated by the vertical portions of the data in (f). Specifically, the first vertical line at $t \approx 6000$ s relates to all of the yellow droplets in (c) that exit at nearly the same time. Again, the existence of avalanches despite the constant flux set by the syringe pump shows that there is some compliance in the plumbing, such that the pressure builds up before an avalanche.

Fig. 2(g)-(i) show the histograms of exiting flux. The exiting flux size is the number of droplets exiting during a time window T , with T chosen to make the mean flux size to be 10. The smooth flow case (g) has a Gaussian shape while the avalanche case (i) has a few rare but large events. To quantify this, the skewness values for these distributions are (g) 0.15, (h) -0.03, and (i) 2.2 for smooth flow, intermediate, and avalanche cases respectively. Not surprisingly, the avalanche case has a large positive skewness, and this is generally true that all avalanche flow cases have positively skewed distributions. Given that the avalanche cases have very few events overall, our skewness data are noisy and we cannot resolve any clear trend in the skewness as a function of our control parameters. The general picture shown in Fig. 2(g)-(i) is clear, though, that avalanche cases have distributions with positive skewness and there is a trend toward more symmetric distributions with skewness ≈ 0 as F increases.

To better quantify the difference of these flow behaviors, we introduce a method focusing on the temporal behavior of the flow. In avalanche cases, discrete sudden flow events are separated by time intervals where droplets barely move and no droplets exit the hopper. Accordingly, we define the time between two successive droplets exiting the hopper as the interval Δt . As shown in Fig. 3, we set t_1 as the time when the black droplet exits the hopper, t_2 as the time when the next droplet (in red) exits, and then $\Delta t = t_2 - t_1$.

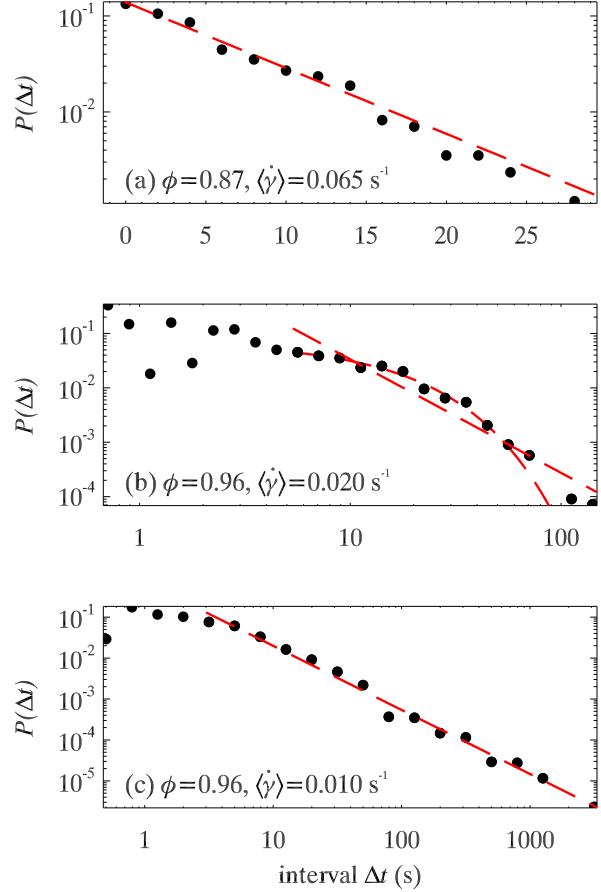


Fig. 4 Typical examples of three types of probability distribution functions of Δt : (a) exponential distribution, (b) intermediate case, (c) power law distribution. The area fraction ϕ and mean strain rate $\langle \dot{\gamma} \rangle$ are as indicated in each panel. In (a) the line shows an exponential fit $P(\Delta t) \sim e^{-\Delta t/\tau}$ with $\tau = 6.3$ s. In (b) the straight line is a power-law fit $P(\Delta t) \sim \Delta t^{-\alpha}$ with $\alpha = 2.1$ and the curved line is an exponential fit with $\tau = 12.7$ s. In (c) the line is a power-law fit with $\alpha = 1.6$.

It is apparent in the plots in Fig. 2(d-f) that the distributions of Δt are different for the smooth flow and avalanche cases. In smooth flow, the values of Δt are small and do not fluctuate much. In the avalanche case, Δt is sometimes small (vertical portions, where many droplets exit over a short time interval) and sometimes large (horizontal stretches, where a long time passes between one droplet exiting and the next). Figure 4 shows the probability distribution functions for Δt for the same three data sets shown in Fig. 2. The smooth flow case shown in Fig. 4(a) is well fit to an exponential, as shown by the dashed red line; note this is a semilog plot. The exponential fit $P(\Delta t) \sim e^{-\Delta t/\tau}$ defines the mean time between events τ , and the fit suggests that the time between events follows a Poisson process, where events occur continuously and independently

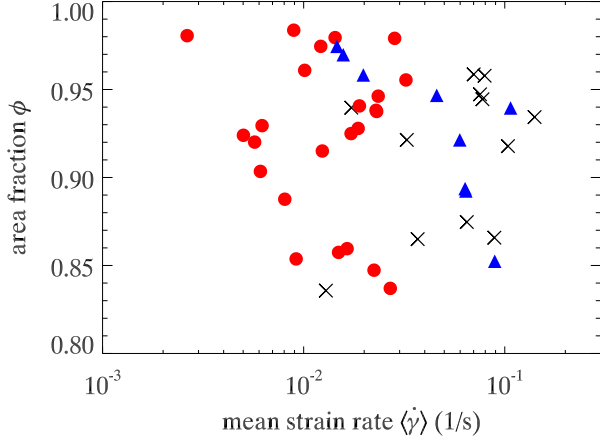


Fig. 5 Phase diagram of fitting patterns of $P(\Delta t)$ in terms of area fraction ϕ and mean strain rate $\langle \dot{\gamma} \rangle$. Red circle: power law; blue triangle: intermediate; black cross: exponential.

with a constant mean rate. The avalanche case shown in panel (c) is well fit to a power law, as shown by the dashed red line; note this is a log-log plot. The fit in this case is given by $P(\Delta t) \sim \Delta t^{-\alpha}$ with $\alpha = 1.6$, and the power law regime covers more than 2 decades in Δt and more than 4 decades in probability. The tails correspond to the long periods of time where droplets barely move. The intermediate case in panel (b) is plotted on log-log axes, and can be fit with either a power law (straight line) or an exponential (curved line); neither fit is perfect. The exponential fit fails for the largest Δt while the power law is not adequate to describe the small Δt region.

In our experiments we have varied both ϕ and flux rate (quantified by the mean strain rate $\langle \dot{\gamma} \rangle$). For each experiment, we use the shape of $P(\Delta t)$ to describe its flow behavior. Figure 5 shows the phase diagram of fitting patterns. There is no obvious trend with ϕ , but more clearly a transition from avalanche flow (red circles) to avalanche flow (black cross) with increasing $\langle \dot{\gamma} \rangle$. Note that the judgment about the best fitting function is done by eye. The quality of each fit depends on which range of data is used for the fit, and while we have tried several ways to approach the fitting procedure more systematically, none seem satisfactory for the intermediate cases, and none affect the appearance of Fig. 5 in any substantial way.

The phase diagram of Fig. 5 is perhaps unsatisfying as the intermediate cases (blue triangles) are mixed in with the other two cases. However, by ignoring ϕ and focusing only on the flow rate dependence, the data become more unified. In particular, Fig. 6(a) shows the relation between the power law exponent of $P(\Delta t)$ and $\langle \dot{\gamma} \rangle$. The power exponent α increases as the mean strain rate increases. Even when the power law fit is not perfect (triangles), the data still follow the general trend started by the well-fit power law cases (circles). Smaller values of α indicate a broader distribution, where the large Δt

events are more significant: these are the avalanche cases with long pauses between short bursts when many droplets exit. This is similar to previous experimental studies of sheared granular materials, where they have power law distributions of various stick-slip event properties including forces, energy, and avalanche sizes^{21,30–34}.

To consider the exponential cases, we note that the exponential fitting parameter τ corresponds to the mean interval. Accordingly, in Fig. 6(b) we compute $\langle \Delta t \rangle$ for every experiment (no matter the distribution shape) and see that this decreases as mean strain rate $\langle \dot{\gamma} \rangle$ increases. This is plausible since the strain rate is bigger for higher flow velocity and thus droplets exit faster, which leads to small mean interval. Note that for those cases in Fig. 6(a) with $\alpha < 2$, it is problematic to define $\langle \Delta t \rangle$ since the mean of a power law distribution with $\alpha < 2$ is infinite. Thus, our finite values of $\langle \Delta t \rangle$ merely reflect the finite amount of data. It is plausible that the power law distributions may well have some cutoff at very large Δt . To an extent, the relationship shown in Fig. 6(b) is trivial by dimensional analysis: $\langle \Delta t \rangle$ and $\langle \dot{\gamma} \rangle^{-1}$ have dimensions of time. The dashed red line in Fig. 6(b) is a power law fit with exponent -1.2 , fairly close to the -1 suggested by dimensional analysis. The different exponent, and the reason the data don't completely collapse, is that the two quantities are different averages: in general $\langle x \rangle \neq \langle x^{-1} \rangle^{-1}$ and in specific $\langle \Delta t \rangle$ focuses on droplets exiting whereas $\langle \dot{\gamma} \rangle$ focuses on the behavior of all of the droplets everywhere, averaged over both time and space.

4 Conclusions

We have demonstrated that in a single experimental geometry, we see behaviors changing from clear avalanches to smooth continuous flows as we increase the mean flow rate by a factor of 100. We quantify these behaviors by examining the distributions of times Δt between subsequent droplets exiting the hopper. Intriguingly, the transition in the flow behaviors is somewhat smooth as we increase the flow rate: the power law exponent characterizing the tails of $P(\Delta t)$ smoothly varies as the flow rate increases past the point where a power law no longer adequately describes the data. One possibility is that at any flow rate, the distribution $P(\Delta t)$ may be describable by a power law with an exponential cutoff, and this cutoff may smoothly move to smaller Δt as the flow rate increases. However, the data we have for the intermediate cases [such as shown in Fig. 4(b)] are hard to interpret in the tails, and so it is difficult to resolve this question. The rate dependence of our observations is consistent with prior studies of athermally sheared 2D amorphous solids which demonstrated rate dependence^{18,35–40}. The dependence on velocity is also displayed in experimental works on sheared granular materials, where friction plays a key role^{9,10}. For hopper flow in granular experiments, the presence of static friction can make jamming and

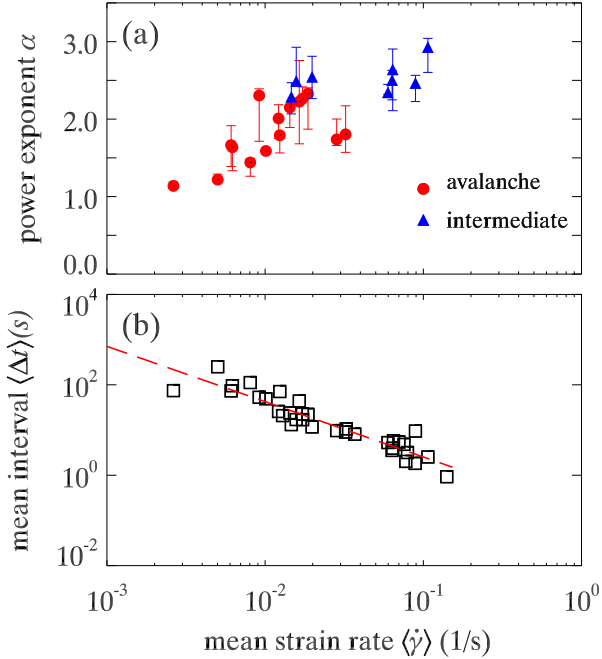


Fig. 6 (a) The power law exponent α as a function of mean strain rate $\langle \dot{\gamma} \rangle$. For the power law fits, only data in the tail are used for the fit. Different choices of the minimum Δt used for the fit give rise to different values of α , reflected in the error bars shown here. (b) Mean interval $\langle \Delta t \rangle$ as a function of $\langle \dot{\gamma} \rangle$. The dashed line is a fit with slope of -1.2.

clogging obvious, where stress-supporting solid arches form across the exit⁴¹. In addition to static friction, such experiments are also driven by a constant force (gravity), whereas in our experiments the syringe pump increases the pressure until flow occurs, and so no arches can persist indefinitely.

The transition from avalanche to smooth flow happens around $\langle \dot{\gamma} \rangle \approx 0.02 \text{ s}^{-1}$, indicated in Fig. 5. While we use mean strain rate to indicate each data set, actually the strain rate is spatially inhomogeneous. Within the imaged field of view, $\dot{\gamma}$ near the hopper exit can be 5 to 14 times bigger than the mean strain rate $\langle \dot{\gamma} \rangle$. Thus at the hopper exit using this local $\dot{\gamma}$, the transition point is $\dot{\gamma} \approx 0.1 \text{ s}^{-1}$ to 0.28 s^{-1} . The inverse of this gives us a time scale $\tau_\gamma = 1/\dot{\gamma}$ about 3.6 to 10 seconds. τ_γ is the time for the system to strain by 1, which microscopically can be viewed as the time for one droplet to slide past a neighboring droplet. In a 2D system, the simplest topological rearrangement is the neighbor exchange of a group of four droplets, known as a T1 event^{17,26}: two droplets that are neighbors move apart, and between them two droplets that weren't neighbors before move together and become neighbors. The time scale of a T1 event τ_{T1} in our system is a few seconds²⁶. This is determined from the mean structural relaxation time based on the change of local stress field around

a T1 event⁴². So, for fast flow rates in our experiment, a rearrangement event near the hopper exit which allows one droplet to exit may not be fully completed before the next rearrangement happens, allowing for substantial cross-talk between given events²⁶. At slower flow rates, individual events can be less correlated, allowing fewer droplets to exit at a time, until the stress builds up and is released in a large avalanche event where many rearrangements happen nearly simultaneously. In our intermediate cases, it may be that in some moments rearrangement events occur close enough in space and time to influence and enhance each other, whereas in other moments events are more individual; some evidence of this has been seen in simulations of 2D foam flow⁴³ and other systems³⁶.

In summary, we see that the flow of an emulsion through a hopper can vary from avalanche-like to continuous. The transition between these behaviors is not abrupt, but rather a continuous function of the flow rate. At the lowest flow rates, the power law exponent we observe approaches $\alpha = 1$, showing that the flow has extremely long quiescent intervals in between the avalanches. The decrease of the power law exponent with decreasing flow rate [Fig. 6(a)] suggests that even with these slow flows, we are not in a quasi-static limit, in agreement with a prior study of slowly sheared bubble rafts⁴⁴. In this simple limit where the strain rate approaches zero, the flow is not simple, but rather dominated by the rare intermittent avalanches.

Acknowledgments

This work was financially supported by NSF grant NSF(CBET-1336401) and Petroleum Research Fund (47970-AC9), administered by the American Chemical Society. We thank K. Dahmen, C. Orellana, and I. Zuriguel for helpful discussions.

References

- 1 R. Benzi, M. Sbragaglia, P. Perlekar, M. Bernaschi, S. Succi and F. Toschi, *Soft Matter*, 2014, **10**, 4615–4624.
- 2 A. D. Gopal and D. J. Durian, *Phys. Rev. Lett.*, 1995, **75**, 2610–2613.
- 3 M. Dennin and C. M. Knobler, *Phys. Rev. Lett.*, 1997, **78**, 2485–2488.
- 4 S. Tewari, D. Schiemann, D. J. Durian, C. M. Knobler, S. A. Langer and A. J. Liu, *Phys. Rev. E*, 1999, **60**, 4385–4396.
- 5 J. P. Sethna, K. A. Dahmen and C. R. Myers, *Nature*, 2001, **410**, 242–250.
- 6 D. Fisher, K. Dahmen, S. Ramanathan and Y. Ben-Zion, *Phys. Rev. Lett.*, 1997, **78**, 4885–4888.
- 7 K. Dahmen, D. Ertaş and Y. Ben-Zion, *Phys. Rev. E*, 1998, **58**, 1494–1501.
- 8 K. A. Dahmen, Y. B. Zion and J. T. Uhl, *Phys. Rev. Lett.*, 2009, **102**, 175501.
- 9 S. Nasuno, A. Kudrolli and J. Gollub, *Phys. Rev. Lett.*, 1997, **79**, 949–952.
- 10 J. Krim, P. Yu and R. P. Behringer, *Pure and Applied Geophysics*, 2011, **168**, 2259–2275.

-
- 11 J. Urbach, R. Madison and J. Markert, *Phys. Rev. Lett.*, 1995, **75**, 276–279.
 - 12 I. Zuriguel, D. R. Parisi, R. C. Hidalgo, C. Lozano, A. Janda, P. A. Gago, J. P. Peralta, L. M. Ferrer, L. A. Pugnaloni, E. Clément, D. Maza, I. Pagonabarraga and A. Garcimartín, *Scientific Reports*, 2014, **4**, 7324.
 - 13 M. Dennin, *Phys. Rev. E*, 2004, **70**, 041406.
 - 14 D. J. Durian, *Phys. Rev. E*, 1997, **55**, 1739–1751.
 - 15 E. Pratt and M. Dennin, *Phys. Rev. E*, 2003, **67**, 051402.
 - 16 Y. Bertho, C. Becco and N. Vandewalle, *Phys. Rev. E*, 2006, **73**, 056309.
 - 17 M. Lundberg, K. Krishan, N. Xu, C. S. O’Hern and M. Dennin, *Phys. Rev. E*, 2008, **77**, 041505.
 - 18 R. R. Hartley and R. P. Behringer, *Nature*, 2003, **421**, 928–931.
 - 19 A. Janda, I. Zuriguel, A. Garcimartín, L. A. Pugnaloni and D. Maza, *Europhys. Lett.*, 2008, **84**, 44002.
 - 20 M. A. Aguirre, J. G. Grande, A. Calvo, L. A. Pugnaloni and J. C. Géminard, *Phys. Rev. Lett.*, 2010, **104**, 238002.
 - 21 N. Hayman, L. Ducloué, K. Foco and K. Daniels, *Pure and Applied Geophysics*, 2011, **168**, 2239–2257.
 - 22 P. Lafond, M. Gilmer, C. Koh, E. Sloan, D. Wu and A. Sum, *Phys. Rev. E*, 2013, **87**, 042204.
 - 23 T. J. Wilson, C. R. Pfeifer, N. Mesyngier and D. J. Durian, *Papers in Physics*, 2014, **6**, 060009.
 - 24 J. Rajchenbach, *Phys. Rev. Lett.*, 1990, **65**, 2221–2224.
 - 25 K. W. Desmond, P. J. Young, D. Chen and E. R. Weeks, *Soft Matter*, 2013, **9**, 3424–3436.
 - 26 D. Chen, K. W. Desmond and E. R. Weeks, *Soft Matter*, 2012, **8**, 10486–10492.
 - 27 R. Shah, H. Shum, A. Rowat, D. Lee, J. Agresti, A. Utada, L. Chu, J. Kim, A. Fernandez-Nieves and C. Martinez, *Materials Today*, 2008, **11**, 18–27.
 - 28 J. C. Crocker and D. G. Grier, *J. Colloid Interface Sci.*, 1996, **179**, 298–310.
 - 29 M. D. Haw, *Phys. Rev. Lett.*, 2004, **92**, 185506.
 - 30 K. A. Dahmen, Y. Ben-Zion and J. T. Uhl, *Nat Phys*, 2011, **7**, 554–557.
 - 31 R. Candelier, O. Dauchot and G. Biroli, *Phys. Rev. Lett.*, 2009, **102**, 088001.
 - 32 J. Zhang, T. S. Majmudar, A. Tordesillas and R. P. Behringer, *Granular Matter*, 2010, **12**, 159–172.
 - 33 T. S. Majmudar and R. P. Behringer, *Nature*, 2005, **435**, 1079–1082.
 - 34 A. Baldassarri, F. Dalton, A. Petri, S. Zapperi, G. Pontuale and L. Pietronero, *Phys. Rev. Lett.*, 2006, **96**, 118002.
 - 35 A. Lemaître and C. Caroli, *Physical Review Letters*, 2009, **103**, 065501.
 - 36 R. White and K. Dahmen, *Phys. Rev. Lett.*, 2003, **91**, 085702.
 - 37 G. Katgert, M. Möbius and M. van Hecke, *Phys. Rev. Lett.*, 2008, **101**, 058301.
 - 38 K. Krishan and M. Dennin, *Phys. Rev. E*, 2008, **78**, 051504.
 - 39 D. Howell, R. P. Behringer and C. Veje, *Phys. Rev. Lett.*, 1999, **82**, 5241–5244.
 - 40 C. Veje, D. Howell and R. Behringer, *Phys. Rev. E*, 1999, **59**, 739–745.
 - 41 K. To, P. Y. Lai and H. K. Pak, *Phys. Rev. Lett.*, 2001, **86**, 71–74.
 - 42 K. W. Desmond and E. R. Weeks, *arXiv:1306.0269*, 2013.
 - 43 Y. Jiang, P. J. Swart, A. Saxena, M. Asipauskas and J. A. Glazier, *Phys. Rev. E*, 1999, **59**, 5819–5832.
 - 44 M. Twardos and M. Dennin, *Phys. Rev. E*, 2005, **71**, 061401.